

Analysis of Surface and Interior Permanent Magnet Motor Topologies for Active Electromagnetic Damping Applications

Original

Analysis of Surface and Interior Permanent Magnet Motor Topologies for Active Electromagnetic Damping Applications / Aguilar-Zamorate, Irving S.; Galluzzi, Renato; Ibarra, Luis; Amati, Nicola; Soriano, Luis Arturo. - In: MACHINES. - ISSN 2075-1702. - 11:7(2023). [10.3390/machines11070721]

Availability:

This version is available at: 11583/2990817 since: 2024-07-15T09:08:50Z

Publisher:

MDPI

Published

DOI:10.3390/machines11070721

Terms of use:






This article is made available under terms and conditions as specified in the corresponding bibliographic description in the repository

Publisher copyright

(Article begins on next page)

Article

Analysis of Surface and Interior Permanent Magnet Motor Topologies for Active Electromagnetic Damping Applications

Irving S. Aguilar-Zamorate ¹, Renato Galluzzi ^{1,*}, Luis Ibarra ², Nicola Amati ³
and Luis Arturo Soriano ⁴

¹ School of Engineering and Sciences, Tecnológico de Monterrey, Mexico City 14380, Mexico; a01336855@tec.mx

² Institute of Advanced Materials for Sustainable Manufacturing, Tecnológico de Monterrey, Mexico City 14380, Mexico; ibarra.luis@tec.mx

³ Center for Automotive Research and Sustainable Mobility (CARS), Politecnico di Torino, 10129 Turin, Italy; nicola.amati@polito.it

⁴ Departamento de Ingeniería Mecánica Agrícola, Universidad Autónoma Chapingo, Texcoco 56235, Mexico; lsorianoa@chapingo.mx

* Correspondence: renato.galluzzi@tec.mx

Abstract: Many modern high-end vehicles exploit controllable damping solutions to enhance their adaptability to different road conditions and driving styles. Among these technologies, active dampers offer improved performance due to their four-quadrant operation in the torque–speed plane. In active electromagnetic dampers, brushless permanent magnet machines are used because of their high torque density. However, to the best of our knowledge, a process to set the previously reported; likewise, which rotor topology exhibits the best performance in such cases has not been validated. Consequently, the resulting actuator could exhibit suboptimal dynamical performance and power conversion efficiency. Although some design processes have been formulated in the past for semiactive controllers (the damping is modified using a variable resistive load), they are not suitable for active suspension control. Similarly, there are existing solutions to increase conversion efficiency using mechanical motion rectifiers; however, active forces cannot be exerted, limiting their applicability to semiactive actuators. Therefore, this paper presents a design methodology, using finite element method together with MATLAB/Simulink™, to set and test the parameters of AC brushless PM machines, intended for actively controlled suspensions. A novel approach to set the base speed, which takes advantage of field-weakening capability, is also presented. To test the proposed method, three machines with well-known rotor topologies were designed and evaluated as case studies, and the surface-mounted topology was found to be the most suitable for the analyzed task.

Keywords: electromagnetic dampers; field-oriented control; active suspensions; permanent magnet synchronous machines; brushless permanent-magnet motors



Citation: Aguilar-Zamorate, I.S.; Galluzzi, R.; Ibarra, L.; Amati, N.; Soriano, L.A. Analysis of Surface and Interior Permanent Magnet Motor Topologies for Active Electromagnetic Damping Applications. *Machines* **2023**, *11*, 721. <https://doi.org/10.3390/machines11070721>

Academic Editor: Ahmed Abu-Siada

Received: 27 May 2023

Revised: 24 June 2023

Accepted: 6 July 2023

Published: 7 July 2023



Copyright: © 2023 by the authors. Licensee MDPI, Basel, Switzerland. This article is an open access article distributed under the terms and conditions of the Creative Commons Attribution (CC BY) license (<https://creativecommons.org/licenses/by/4.0/>).

1. Introduction

Through recent years, the automotive sector has overseen substantial growth in the inclusion of smart, electrified chassis features. In this industry, mechatronic actuators are used to develop the so-called *x-by-wire* solutions, and they are planned to replace purely mechanical or hydraulic systems in the near future. This choice is motivated by key improvements in performance, reliability, and economical benefits [1]. Controlled suspensions can be related to these technologies; they allow the vehicle to adapt to diverse driving conditions while enhancing ride quality in terms of passenger comfort and road holding by tires [2]. The interest in controllable suspension has been rekindled by efforts to develop automated driving systems, which have pushed the requirements of vehicle dynamics objectives to stricter levels.

Electromagnetic shock absorbers rely on electric machines to provide suspension operation in the active and passive quadrants, with intrinsic reversibility, favorable con-

trollability, and regenerative capabilities. In addition, they can be easily integrated in an electrified chassis, where the bidirectional energy interaction can be adapted to the vehicle battery system.

Although linear motors offer better adaptability to suspension kinematics, these devices are higher cost, and have a large volume and mass and limited force output. In contrast, rotary electric motors can be fitted into typical suspension architectures via proper mechanical or hydrostatic transmissions that convert linear motion into rotation. Multiple works have demonstrated that these rotary configurations outperform their linear motor counterparts in suspension systems [3].

Brushless permanent magnet (PM) machines have widespread use in applications where high power and torque density are paramount. Accordingly, this type of motor is increasingly being used in industrial and transport systems [4] due to its reliability, smooth operation, and extended range above the base speed (field-weakening capability). So, the use of brushless PM motors in electromagnetic dampers is a clear choice [5].

To yield optimal performance, the design of the electric machine should be tailored for the application. Although some electromagnetic damper design guidelines are available in the literature [6], they are inherent to the passive quadrants of operation. In [5], the parameters for an AC brushless motor were defined to satisfy a maximum damping specification. However, the field-weakening capability was not explored. Another important aspect, heretofore unexplored, is the rotor topology, specifically evaluating the selection of surface-mounted (SPM) or interior PM (IPM) rotors in this context. These details have been studied for electric traction applications [7], but remain unstudied in electromagnetic dampers.

This paper presents the design process of brushless PM motors, also called PM synchronous motors (PMSMs), for electromagnetic dampers. SPM, V-shape IPM, and flat IPM topologies were studied to identify the most suitable choice for the target application. Torque and speed requirements were defined from a worst-case duty profile of the motor when used as a full active damper operating in the four quadrants of the torque–speed plane. An optimization process was carried out to maximize output torque, while accounting for the magnetic and geometric constraints of the machine. This approach exploited the integration between Finite Element Method Magnetics (FEMM) and MATLAB™. FEMM was used as a simulation tool to evaluate the stationary performance of the machine. MATLAB™ triggered FEMM through a minimization algorithm, where machine features were varied while converging to an optimal solution. This seamless integration was performed through the OctaveFEMM function set. The performance of the three optimized machine architectures was analyzed in a vehicle suspension model with a realistic mission profile, considering the added energy consumption from inertia and the friction damping of the rotating parts. Field weakening was used to operate the machine during peak speed transient periods.

The remainder of this paper is organized as follows. In Section 2.1, system requirements are established from vertical vehicle dynamics while applying an active suspension control strategy. Then, Section 2.2 describes the geometric and winding features for the stator and each of the rotor topologies. The optimization process is detailed in Section 2.3. Subsequently, each optimal machine configuration is characterized using field-oriented control; loss and efficiency maps are calculated (Section 2.4). Later, the performance of the different machine topologies is analyzed and compared for the use case in Section 2.5. The results are presented and discussed in Section 3. Last, Section 4 concludes the work.

2. Design

The electric machine, the target of this design, was assumed to be integrated inside an electromagnetic shock absorber for full active suspension control. Given the nature of suspension motion, a mechanism is necessary to convert linear displacements into rotation.

Many options are possible in this context [3]. However, for the purpose of this study, an ideal transmission ratio can be defined as

$$\tau_t = \frac{\dot{z}_d}{\omega_m} \quad (1)$$

where ω_m is the mechanical angular speed of the electric machine, and \dot{z}_d is the actuator speed. For this application, $\tau_t = 1.32$ mm/rad; this value was obtained from a previously designed actuator [5]. Similarly, the actuator force F_a is directly proportional to the motor torque T_m :

$$F_a = \frac{T_m}{\tau_t}. \quad (2)$$

These simple relationships allow mapping suspension force and linear velocity requirements into torque and angular speed.

2.1. System Requirements from Vehicle Dynamics

The performance of a regenerative damper was analyzed through the vertical dynamics of a passenger vehicle using a quarter-car model (Figure 1). In this case, the traditional damper was replaced with an ideal active actuator that represents the electromagnetic shock absorber. The expressions that govern this system are

$$m_s \ddot{z}_s + k_s(z_s - z_u) - F_a = 0 \quad (3)$$

$$m_u \ddot{z}_u + k_s(z_u - z_s) + k_u(z_u - z_r) + F_a = 0 \quad (4)$$

where labels s,u denote the sprung (chassis) and unsprung (wheel hub) bodies, respectively. Generalized coordinates are denoted with $z_{s,u}$, whereas body masses are given by $m_{s,u}$. Parameters k_s and k_u are the stiffness of the suspension spring and the tire, respectively. The input z_r is the road roughness vertical displacement profile, while F_a is the active force provided by the damper.

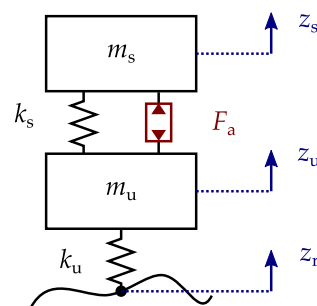


Figure 1. Scheme of a quarter car. The traditional damper is replaced with an ideal force actuator.

The quarter-car model was simulated in MATLAB/Simulink™ using the parameters listed in Table 1. The vehicle features belonged to the C-class vehicle template in the automotive software CarSIM™. To ensure proper sizing, the road class and vehicle longitudinal speed were selected to generate worst-case road unevenness. This choice leads to severe activity on the electric machine. A classical suspension control based on mixed skyhook–groundhook strategies [8] was applied. Thus, the active force reference is given by

$$F_{a,ref} = -c_{sky}\dot{z}_s + c_{gnd}\dot{z}_u \quad (5)$$

where c_{sky} and c_{gnd} are the tunable skyhook and groundhook damping coefficients, respectively.

Table 1. Simulation parameters of the quarter-car model.

Parameter	Symbol	Value	Unit
Sprung mass	m_s	413.5	kg
Unsprung mass	m_u	66.3	kg
Spring stiffness	k_s	29.36	kN/m
Tire stiffness	k_u	268	kN/m
Suspension stroke limits	–	± 50	mm
Vehicle longitudinal speed	–	70	km/h
Road roughness index (ISO-C)	–	25.6×10^{-7}	m·cycle
Actuator force limits	–	± 2	kN
Actuator bandwidth	–	1	kHz

The sprung mass acceleration was used to assess passenger comfort; it was filtered by a third-order bandpass filter that amplifies human-sensitive frequencies [9], according to the ISO 2631 standard [10]. Likewise, tire road holding was determined by the so-called road-holding index, i.e., the ratio between the tire elastic force and the corner weight [11]:

$$\eta_{rh} = \frac{k_u(z_u - z_r)}{(m_s + m_u)a_g} \quad (6)$$

where a_g is the gravity acceleration.

The simultaneous optimization of comfort and road holding is not possible because there is an intrinsic trade-off between them in a passenger car [8]. Therefore, the optimal gains for c_{sky} and c_{gnd} were found by minimizing the root mean square (rms) weighted (filtered) chassis acceleration a_w or the road-holding index η_{rh} . In both cases, the suspension stroke $z_d = z_s - z_u$ was constrained to its mechanical limits, whereas the road-holding index was restricted below unity to avoid wheel detachment from the ground. The control gains and their respective metrics are outlined in Table 2.

Table 2. Optimal suspension operating points considering the classic control approach.

Condition	c_{sky} [kNs/m]	c_{gnd} [kNs/m]	rms (a_w) [m/s ²]	rms (η_{rh}) [–]	rms (F_a) [N]
Comfort	11.133	1.056	0.83	0.30	499.5
Road holding	3.072	3.292	1.48	0.22	635.5

Then, the actuator design parameters were based on the following considerations. Firstly, continuous actuation force was obtained from rms(F_a) in the worst-case condition (road holding); thus, $F_{cont} = 635.5$ N. This force can be related to the continuous operation of the electric machine. Considering an air-cooled device through natural convection, the actuator should exert this force while supplied by a current density rms(J_{cont}) = 6 A/mm² [12]. Secondly, the motor speed was selected by analyzing the effect of field weakening on vehicle dynamics, unlike previous studies in the literature omitting flux-weakening operation [5].

To this end, the ideal force actuator on the quarter-car model was dynamically saturated according to

$$F_{sat}(v) = \begin{cases} F_{cont}k_J & \text{if } |v| \leq v_b \text{ Constant force region} \\ F_{cont}k_J \frac{v_b}{v} & \text{if } |v| > v_b \text{ Constant power region} \end{cases} \quad (7)$$

where $v = \dot{z}_d$ is the actuator speed. The actuator base speed v_b represents the limit between the constant force and the constant power regions. A coefficient $k_J = 3.3$ was included to account for the overload capability of the machine in transient conditions (less than ten seconds). Hence, a suitable base speed must be selected to set the field-weakening region

boundary to the machine without hindering the dynamic response of the vehicle. Note that the machine sizing is based on current density limitations following the empirical thermal performance available in the literature [12]. A dedicated thermal model is needed to properly assess this point. However, in the given application, the set up of such model is very complex due to the uncertainty of heat sources, such as the vehicle engine, the brake calipers, and the airflow running through the wheel arch, among others. Although these details are of relevance and interest, they are beyond the scope of the present study.

The results in Figure 2 illustrate the effect of changing v_b on both the suspension stroke and theroad-holding index limits. These values should not exceed the established restrictions: $\max(|\eta_{rh}|) \leq 1$, $\max(|z_d|) \leq 50$ mm. Base speed values above 0.54 m/s led to suspension stroke and road-holding index values that fulfilled the aforementioned constraints. Thereby, this value was selected as the base speed for the electric machine design.

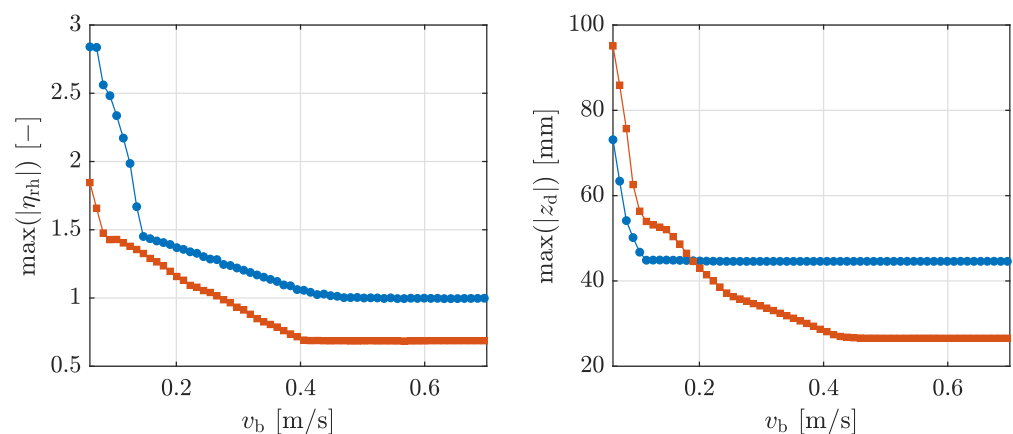


Figure 2. Suspension stroke and road-holding index limits while varying the base speed v_b . Two control strategies were considered: optimal comfort (circle) and road holding (square).

Finally, applying (2) and (1), the force and linear speed values were converted to torque and angular speed targets: $T_{\text{cont}} = 0.84$ Nm, $\omega_b = 3907$ rpm. Figures 3 and 4 show the electric machine activity within the suspension when controlled with the optimal comfort and road holding strategies. Remember that the obtained suspension activity comes from a worst-case simulation where the vehicle runs at 70 km/h on an ISO-C road profile. In this condition, the actuator rarely works in the field-weakening region. The comfort strategy operates in field weakening 5.4% of the time. For the road-holding strategy, field weakening takes place only 0.2% of the time. It is worth noting that although field weakening is rarely used in normal vehicle operation, rare situations, such as traveling over a bump or pothole, push the suspension to speeds in excess of 10 krpm. Then, the machine should be able to enter the field-weakening region in these extreme cases.

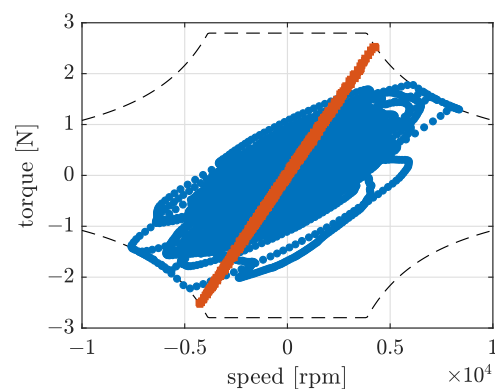


Figure 3. Optimal comfort (circle) and road-holding (square) strategies at the motor level: torque versus angular speed. The theoretical field-weakening limit (dashed) is also outlined.

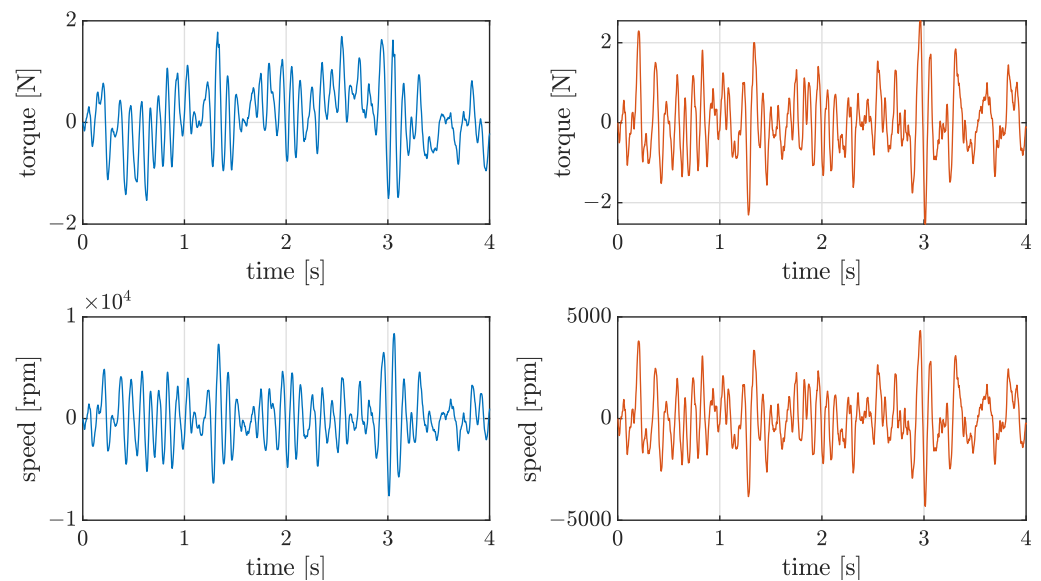


Figure 4. Optimal comfort (right) and road-holding (left) strategies at the motor level: torque and angular speed–time histories.

2.2. Machine Geometry and Winding Scheme

In a suspension, compactness is key to guaranteeing proper kinematics without interference. In fact, suspension elements share space with other assemblies, such as the brakes and the wheel. For the front axle, the steering must also be taken into account. These constraints are considered in the electric machine design, where the main goal is to maximize the output torque to limit the actuator volume and mass.

To yield a compact electric machine, a fractional-slot motor topology with a double-layer winding was selected. This choice brings multiple advantages. First, these layouts minimize end-turn length, thus leading to a compact machine in terms of the axial envelope and low end-turn Joule losses. Second, fractional-slot layouts exhibit low cogging torque ripple without needing to apply additional mitigation techniques [13].

Different pole–slot combinations are possible for fractional-slot PMSM topologies. These choices lead to different values of the winding factor, which is a measurement of the effectiveness of the magnetic flux linked in the coils [14]. Accordingly, the torque and back electromotive force (EMF) are proportional to the winding factor. In this regard, a twelve-slot, ten-pole PMSM configuration was selected as the base architecture for all the machines in this study. This combination leads to a relatively high winding factor with respect to other alternatives, maintaining a low harmonic content on the back EMF, which has a positive impact on the machine efficiency.

The stator geometry was the same for all the machine designs, although numerical dimensions varied among solutions. As shown in Figure 5, the stator geometry is defined by outside radius R_{so} , back iron radius R_{sb} , back iron width w_{bi} , tooth base width w_{tb} , slot base width w_{sb} , slot inner width w_{si} , tooth width w_t , shoe opening w_s , shoe depth d_1 , tooth-to-shoe depth d_2 , tooth base depth d_3 , and air gap length g . Its winding obeys the fractional-slot topology with two layers per slot, as also illustrated in Figure 5.

On the contrary, rotor topologies did change for the tested machines. IPM geometries present flat and V-shaped magnets. They are depicted in Figure 6. Common parameters are shared among rotor geometries: magnet length l_m , outer rotor radius R_{ro} , and inner rotor radius R_{ri} . The SPM topology is further specified by rotor back iron w_{bi} and magnet fraction $\alpha_m = \tau_m / \tau_p$, where τ_m is the magnet pitch, and τ_p is the pole pitch.

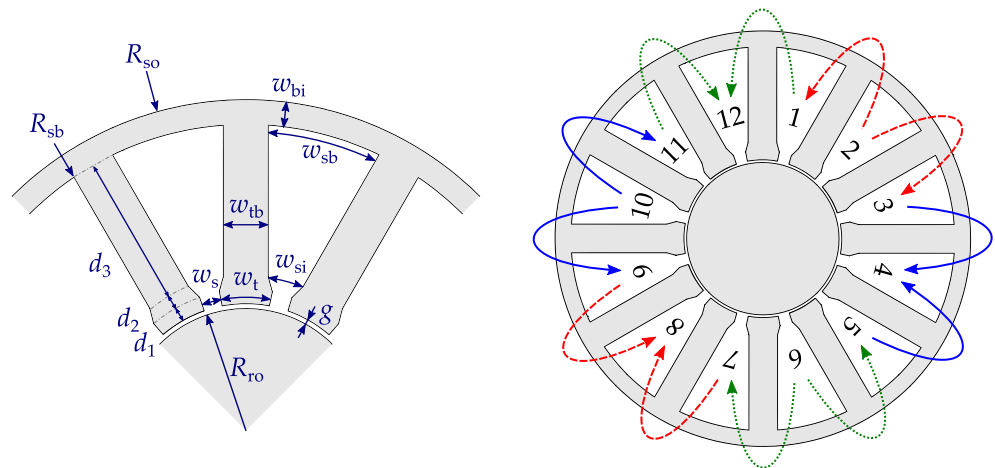


Figure 5. Stator geometry and winding layout for a radial-flux PMSM with twelve slots and ten poles. Phases are denoted by dashed (A), dotted (B), and solid (C) lines.

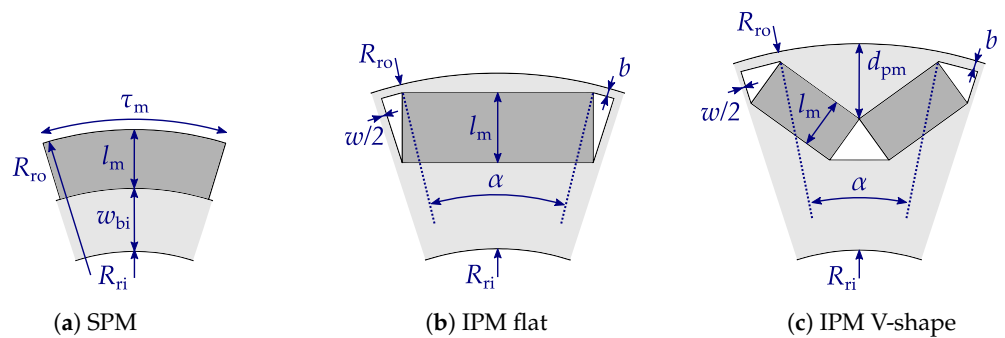


Figure 6. Permanent magnet rotor topologies. Dark and light gray represent PM and iron, respectively.

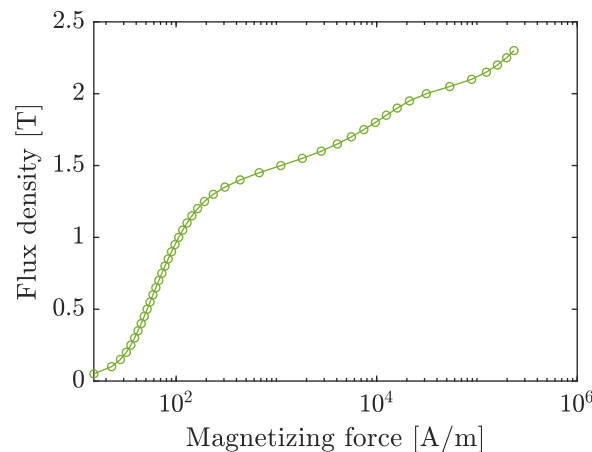
IPM designs share three parameters: magnet opening angle α , web thickness w , and bridge width b . The IPM V-shape has an additional parameter, which is the magnet depth d_{pm} in the radial direction. Dimensions w and b define an iron structure to hold the magnets into the rotor. The presence of this iron material is relevant, especially when the rotor is subject to high centrifugal stress. However, oversizing this structure might lead to a short circuit of the PM paths, which would decrease the air gap flux and, consequently, reduce the output torque of the machine. Therefore, the proposed design procedure focused exclusively on magnetic performance. However, a preliminary centrifugal stress analysis was carried out at 20 krpm on initial IPM cross-sections using Solidworks™. Conservative values of $b = 0.4$ mm and $w > 0.4$ mm were used. These numbers are compliant with the tolerances of the steel lamination stamping process. Specifically, the minimum distance between cut features must be between one and one and a half times the material thickness (0.35 mm for the employed M230-35A steel) [15].

2.3. Optimization Procedure

The motor design process starts by fixing the parameters listed in Table 3. The listed values belong to common design choices and constraints. The magnetization curve for the M250-35A steel is depicted in Figure 7. Then, each machine cross-section (stator and rotor) is optimized to maximize the torque-to-length ratio. In a force actuator, this design choice aims to minimize the mass of the PMSM, which is a desirable feature in automotive mechatronics. Since the actuator mass is added to the wheel hub (unsprung mass), it may hinder the dynamic vertical vehicle performance. This approach differs from those addressing traction applications where the machine performance is evaluated in a wide speed range [16].

Table 3. Fixed design parameters and material properties.

Parameter or Property	Symbol	Value	Unit
Number of magnets	N_m	10	—
Number of slots	N_s	12	—
Number of phases	N_{ph}	3	—
Air gap length	g	0.5	mm
Stator outside radius	R_{so}	35	mm
Slot shoe opening	w_s	2	mm
Shoe depth	d_1	1.5	mm
Tooth-to-shoe depth	d_2	1.5	mm
Stacking factor (M250-35A)	-	0.95	—
PM remanent flux density	B_r	1.14	T
PM recoil permeability	μ_r	1.05	—
PM conductivity (N45)	σ_{pm}	0.67	MS/m
Electrical resistivity (copper)	ρ_{Cu}	2.582×10^{-8}	Ωm
Winding fill factor	k_f	0.3	—

**Figure 7.** Magnetization curve of M250-35A steel.

Torque was evaluated at continuous current density in the maximum torque-per-ampere (MTPA) condition. The average torque value was calculated from the simulation of five rotor positions equally spaced over a stator slot pitch τ_p . The first position was randomly selected within one-fifth of τ_p to minimize fundamental and third-order ripple harmonics [17]. A Dirichlet-type condition was applied to the outer boundary of the air surrounding each machine geometry. No periodicity in the analysis domain was used in this case. A sliding band air gap model in FEMM was used to allow movement without changing the rotor or stator meshes [18]. To speed up computations, a coarse mesh of approximately 6000 triangular elements was used for each simulation. During optimization, the average flux density in the stator teeth and back iron was limited to 1.2 T. At this stage, the winding was simplified as a single turn with the slot fill factor k_f specified in Table 4. The number of turns is defined at a later stage when setting the base speed of the machine. The total length of the machine was normalized to one meter.

The design variables of each topology are summarized in Table 4. They were varied at each iteration due to their significance and impact on the optimization objective, i.e., the output torque. Table 4 also lists the optimized values for these variables. The known effects of the relevant variables are listed next.

The effect of the radius ratio $RR = R_{ro}/R_{so}$ is bi-fold. The rotor arm length and PM surface are directly proportional to the rotor outside radius. In contrast, an increase in this radius decreases the slot area and reduces the magneto-motive force of the machine [19]. The back iron and tooth base width modify the slot area, but their selection is crucial in

defining an unsaturated working point of the stator iron paths. Since the rotor is part of the magnetic circuit path, saturation is crucial therein as well. For this reason, the rotor and stator back iron widths are set as equal in the SPM design. Similarly, for IPM designs, a space between the inner rotor radius R_{ri} and the closest PM point is set to $1.5w_{bi}$. The magnet fraction α_m changes the magnet flux toward the stator and the magnet-to-magnet leakage flux [19]. The role of the angle θ_m is similar in IPM geometries.

The magnet length in the SPM rotor fixes the PM in a safe operating point to avoid demagnetization. To this end, $l_m = 2.4$ mm was selected to set the so-called permeance coefficient at a value of five. Since analytically solving the magnet operating point is difficult for IPM geometries, the magnet length l_m was included as a design variable. Also, the web thickness w was included in both IPM designs because it affects the magnet leakage flux [20]. Lastly, the magnet depth d_{pm} directly affects the air gap flux density [20].

The particle swarm optimization (PSO) algorithm was selected as it is a readily available choice from the Global Optimization Toolbox in MATLAB™. Previous efforts have shown positive results when using this optimization algorithm for electric machinery [21,22]. A custom cost function was designed to perform the following steps:

1. Define a motor geometry in FEMM by using the parameters listed in Table 4.
2. Simulate the motor performance in FEMM.
3. Extract the torque output, the stator back iron, and the tooth base magnetic flux density values.
4. Discard solutions where magnetic flux density values are aboved 1.2 T.

This level of integration is only possible through the OctaveFEMM function set. The PSO algorithm was set up to have a swarm size of 40, self- and social-adjustment weights of 1.49, adaptive inertia in the range [0.1, 1.1], and the termination criterion was set to a relative error of 10^{-2} .

Table 4. Independent design variables for each topology optimization. Optimal values (Opt), lower (Low), and upper (Up) boundaries are indicated.

Design Variable	Symbol [Unit]	SPM			IPM Flat			IPM V-Shape		
		Low	Up	Opt	Low	Up	Opt	Low	Up	Opt
Radius ratio	RR (–)	0.35	0.65	0.37	0.35	0.65	0.49	0.35	0.65	0.48
Back iron width	w_{bi} (mm)	2	4.5	2.6	1	5	2.7	1	5	2.7
Tooth base width	w_{tb} (mm)	4	9	4.7	2	8	5.1	2	8	4.9
Magnet fraction	α_m (–)	0.91	0.99	0.94	–	–	–	–	–	–
Opening angle	θ_m (deg)	–	–	–	18	31	27.4	18	32	23
Magnet length	l_m (mm)	–	–	–	1	3	2.9	1.8	4.5	2.1
Web thickness	w (mm)	–	–	–	0.4	1	0.7	0.4	2	0.4
Magnet depth	d_{pm} (mm)	–	–	–	–	–	–	1	5	3.1

2.4. Motor Mapping

The PMSM model in the direct (d) and quadrature (q) axes and steady-state conditions can be written in terms of flux linkages as follows:

$$v_d = Ri_d - p\omega_m\lambda_q \quad (8)$$

$$v_q = Ri_q + p\omega_m\lambda_d \quad (9)$$

$$T = \frac{3}{2}p[\lambda_d i_q - \lambda_q i_d] \quad (10)$$

where $\lambda_{d,q}$ denotes the axis flux linkages, R is the phase resistance, ω_m is the rotor mechanical speed, p is the number of pole pairs, $v_{d,q}$ indicates the axis voltages, $i_{d,q}$ represents the

axis currents, and T is the electromagnetic torque. In the linear case, flux linkages can be written as

$$\lambda_d = L_d i_d + \lambda_{pm} \quad (11)$$

$$\lambda_q = L_q i_q \quad (12)$$

with inductance terms $L_{d,q}$ and PM flux linkage λ_{pm} . However, flux linkage representation allows mapping the performance of the machine in the presence of saturation. This nonlinear behavior inevitably occurs in overload conditions.

To account for leakage effects, the end turn inductance contribution was added to the flux linkage terms in d, q. The end-turn inductance L_e is calculated through an analytical model [23]:

$$L_e = \frac{3}{4} N_m \mu_0 \tau_{cp} N^2 \ln \left(\frac{\tau_{cp} \sqrt{\pi}}{\sqrt{2k_f A_s}} \right) \quad (13)$$

where τ_{cp} is the mean coil pitch, and A_s is the slot area. For the concentrated coil winding, τ_{cp} is computed as

$$\tau_{cp} = \frac{2\pi}{N_s} R_{sb}. \quad (14)$$

Before mapping the machine operation, the number of turns per coil N was considered in the model. In particular, the following scaling relations are valid:

$$R = R^1 N^2 \quad (15)$$

$$\lambda_{d,q} = \lambda_{d,q}^1 N \quad (16)$$

$$i_{d,q} = i_{d,q}^1 / N \quad (17)$$

The superscripts denote that the parameters were computed with a single turn per coil, as presented in Section 2.3. The resulting resistance, flux linkage, and current are included in Equations (8)–(10).

The machine was controlled using field-oriented control (FOC) with field weakening, based on the maximum torque-per-ampere (MTPA) and maximum torque-per-volt (MTPV) approaches [24]. The process to obtain the FOC maps of the machine is described next.

The dq flux linkage maps were calculated by applying the rms current density vectors to the machine in the range $[0, 20]$ A/mm². These current density vectors led to specific values of $i_{d,q}$. Then, the voltage and torque contributions were computed using the dq model (Equations (8)–(10)). Finally, the maximum torque was found at different mechanical speeds of the machine under the following current and voltage constraints:

$$\sqrt{i_d^2 + i_q^2} \leq i_{max} \quad (18)$$

$$\sqrt{v_d^2 + v_q^2} \leq \frac{v_{dc}}{\sqrt{3}} \quad (19)$$

where i_{max} is the maximum current vector norm, and v_{dc} is the DC link voltage.

The characterization of the motor losses is relevant to estimating its overall efficiency. Hence, copper, iron, and PM loss components were computed using FEMM, automated with MATLABTM. The resistive losses in the windings were computed as

$$P_{Cu} = 6 \text{ rms}(J)^2 A_{slot} k_f \rho_{Cu} (2l_s + l_{et}) \frac{N_s}{N_{ph}} \quad (20)$$

where l_s is the stator length, l_{et} is the total turn-length of a single coil at both ends, $rms(J)$ is the rms current density, and N_s/N_{ph} is the number of coils per phase.

The core and magnet losses were computed with FEMM to measure flux density and vector potential in the dq current grid from the FOC maps. The results were then postprocessed with the Fourier transformation to obtain the net component from signal harmonics [25]. Iron losses were computed according to Bertotti's loss separation model [26]:

$$P_{Fe}(f_0) = \sum_{m=1}^{N_h} \left[k_h(mf_0)B_m^\alpha + k_e(mf_0)^2B_m^2 + k_a(mf_0)^{1.5}B_m^{1.5} \right] \quad (21)$$

where $k_h = 4.68 \times 10^{-3}$ W/kg, $\alpha = 3.701$ and $k_e = 2.26 \times 10^{-6}$ W/kg for the M250-35A steel. The first term inside the summation corresponds to the hysteresis loss (P_h); the second one represents losses due to eddy currents (P_e); the third term describes the excess or anomalous losses (P_a). B_m is the amplitude of the m th harmonic of the flux density, f_0 is the evaluated frequency, and $N_h = 5$ is the total number of harmonics considered. The number of harmonics was determined from a preliminary sensitivity analysis to account for the most significant loss components. For each motor topology, the frequency was evaluated at $f_0 = 64.5$ Hz, i.e., the nominal speed design requirement (see Section 2.1). The results can be extrapolated to any mechanical speed through

$$P_{Fe}(p\omega_m) = P_h \left(\frac{p\omega_m}{2\pi f_0} \right) + P_e \left(\frac{p\omega_m}{2\pi f_0} \right)^2 + P_a \left(\frac{p\omega_m}{2\pi f_0} \right)^{1.5} \quad (22)$$

The magnet losses were calculated from the expression

$$P_{pm}(f_0) = \frac{1}{2} \sum_{m=1}^{N_h} \left[\sigma_{pm}(2\pi m f_0)^2 |J_{c,m}|^2 A_{z,m} \right] \quad (23)$$

where $J_{c,m}$ is the m th harmonic of the constraint current density calculated with the model from [27], $A_{z,m}$ is the m th harmonic of the PM magnetic vector potential out-of-plane component, $N_h = 6$, and $f_0 = 64.5$ Hz. PM losses can be extrapolated to any speed through

$$P_{pm}(p\omega_m) = P_{pm}(f_0) \left(\frac{p\omega_m}{2\pi f_0} \right)^2. \quad (24)$$

Finally, total power losses at any speed are calculated as

$$P_{loss} = P_{Cu} + P_{fe}(p\omega_m) + P_{pm}(p\omega_m). \quad (25)$$

The torque contribution in (10) was corrected by accounting for core and magnet losses:

$$T_m = T - \frac{P_{Fe}(p\omega_m) + P_{pm}(p\omega_m)}{\omega_m} \quad (26)$$

and the net shaft mechanical power is given by

$$P_m = T_m \omega_m. \quad (27)$$

The efficiency of the machine can be calculated according to its operating mode:

$$\eta = \begin{cases} \frac{P_m}{P_m + P_{loss}} & \text{Motor mode} \\ \frac{P_m - P_{loss}}{P_m} & \text{Generator mode.} \end{cases} \quad (28)$$

2.5. Performance Evaluation

The quarter-car model equipped with a full active damper and evaluated in the worst-case road profile (see Section 2.1) was enhanced to evaluate its behavior with a realistic mapped motor. Motor maps were populated by following the approach described in Section 2.4. Furthermore, the rotating parts were modeled with inertial (equivalent mass $m_{eq} = 7.3$ kg) and dissipative (equivalent viscous damping $c_{eq} = 250$ Ns/m) contributions from the previously designed actuator [5].

In addition to vehicle dynamics metrics, the average values of mechanical power, power loss, electrical power, and efficiency were computed. Because the machine worked predominantly in the generator quadrants, the average efficiency was computed in generator mode, as defined in (28).

The flowchart in Figure 8 presents a synthesis of the presented method for design PM synchronous motors in electromagnetic dampers.

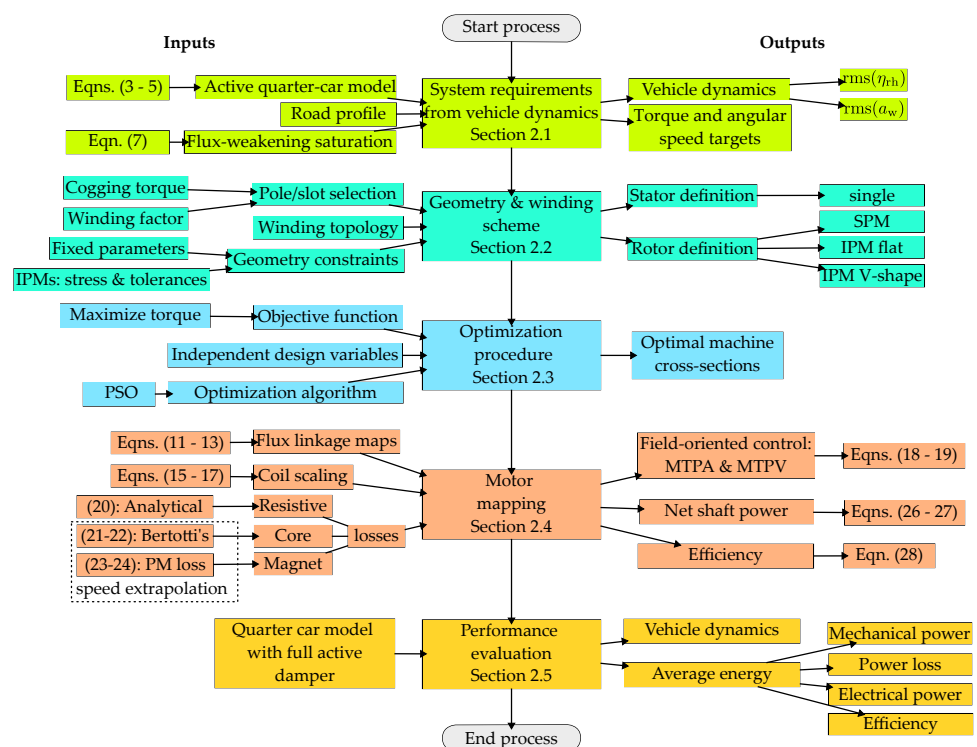


Figure 8. Flowchart of the design methodology for PM synchronous motors (PMSMs) in electromagnetic dampers. The left side shows inputs, while the right side shows the outputs.

3. Results

The described simulations were repeated for the three designed PMSMs. The main performance features of the three machines are summarized in Table 5, from which the following observations were derived. The continuous torque per unit length T_c was the highest in the SPM, in particular, 15.35% and 14.91% greater compared with that of the IPM V-shape and IPM single topologies, respectively. Similar trends were observed for the impulsive torque per unit length. In terms of torque ripple, although the IPM flat design exhibited the lowest torque ripple amplitude ΔT , it showed the same performance as the SPM after normalizing with respect to T_c .

Due to continuous torque being maximized, the main contribution in the constant torque region comes from the magnet torque [28]. Both the SPM and IPM V-shape topologies showed 36% less PM mass than the IPM flat design. Because the IPM designs have a larger radius ratio RR , the effective conduction area and current are less than those of the SPM, even if the SPM has more turns per coil.

Table 5. Performance comparison of three PMSMs. Torque values are expressed per unit length.

Parameter	Symbol	Units	SPM	IPM V-Shape	IPM Flat
Impulsive torque	T_i	Nm/m	74.33	68.25	68.30
Continuous torque	T_c	Nm/m	24.76	21.83	21.38
Torque ripple	ΔT	Nm/m	0.34	0.46	0.29
Relative torque ripple	$\Delta T/T_c$	%	1.39	2.13	1.37
PM mass	—	kg/m	1.27	1.27	1.73
Continuous current amplitude	i_{cont}	A	9.67	9.64	9.30
Impulsive current amplitude	i_{pk}	A	32.2	32.1	31
Number of turns per coil	N	—	17	14	14
Base speed	ω_b	rpm	3976	3949	3893
Active length	l_s	mm	33.5	39.6	39.4

The resulting machine cross-sections and efficiency maps for the three topologies are shown in Figures 9–11. Efficiency maps are plotted in the first (motor) and fourth (generator) quadrants of the plane. These maps are asymmetrical, as expected, due to the different expressions to compute efficiency for each case.

It was observed that the IPM efficiency at high speeds was lower than that of the SPM machine. This is because the PM mass of the IPM rotor topologies is greater than or equal to that of the SPM design, and, thus, the PM losses are similar or larger at higher speeds. Another important aspect to consider is the low saliency ratio ζ of the obtained designs due to the low amount of flux barriers. This demonstrates that the desired small size of the designed machine is a compromise for IPM topologies. In addition, the selection of ten PM poles hindered the saliency ratio. However, this choice was in favor of a high winding factor, as outlined in Section 2.2.

Table 6 compares the three designed machines in the target use case. The three motors exhibited similar comfort and road-holding capabilities. In particular, any of the designs fulfilled $rms(a_w) \leq 0.32$. According to the ISO 2631 standard, the vehicle operation would be deemed as “not uncomfortable” [29]. Road-holding and stroke limits were met as well. Additionally, the rms force, $rms(F_a)$, in the three machine designs with the two strategies is under the continuous torque target, which guarantees an appropriate heat dissipation. In terms of average energy metrics, the IPM designs have the following advantages over the SPM designs: the harvest mechanical power in comfort mode is larger, power losses in road-holding mode are minor, slightly more electrical power is harvested in both optimal modes, and efficiency in road holding mode is superior. Alternatively, the SPM design has these gains over the IPM design: mechanical power in road-holding mode is greater, power losses in comfort mode are lower, and efficiency in comfort mode is higher.

Additionally, all the designs generate more power in road-holding mode than in comfort mode, since the former strategy has a similar dynamic to a passive damper with a high damping coefficient, as shown in Figure 3, so operates almost all the time in regeneration quadrants. However, the average efficiency has an opposite trend because, for the three machines, the maximum efficiency is achieved when operating in comfort mode. This behavior is explained by overlapping the torque–speed curve of the optimal strategies (Figure 3), over the efficiency maps for each motor (Figures 9–11). Then, it was observed that the high damping coefficient (slope) of the road-holding strategy results in operating in regions of medium efficiency, while the most distributed behavior of the comfort strategy with a lower average damping coefficient leads to operating in high- and medium-efficiency regions.

In terms of vehicle dynamics and energy metrics, the SPM, IPM flat, and IPM V-shape topologies have their advantages and drawbacks, which depend on the evaluated active suspension strategy under severe road conditions. However, in terms of compactness, the SPM design is the most favorable topology since it has the highest torque. Additionally, continuous torque can be normalized with respect to the PM mass. In this sense, the

SPM has the highest torque-to-PM mass ratio, with 19.75 Nm/kg; followed by the IPM V-shape, with 16.72 Nm/kg; and, finally, the IPM flat, with 12.34 Nm/kg. Moreover, from the analysis of the active operation in the torque–speed plane in Figure 2, the machine operates most of the time in the constant torque region. Therefore, the predominant reluctance torque contribution in the constant power region from the IPM designs is rarely exploited. For these reasons, the SPM is identified as the best topology for the specified application of electromagnetic dampers.

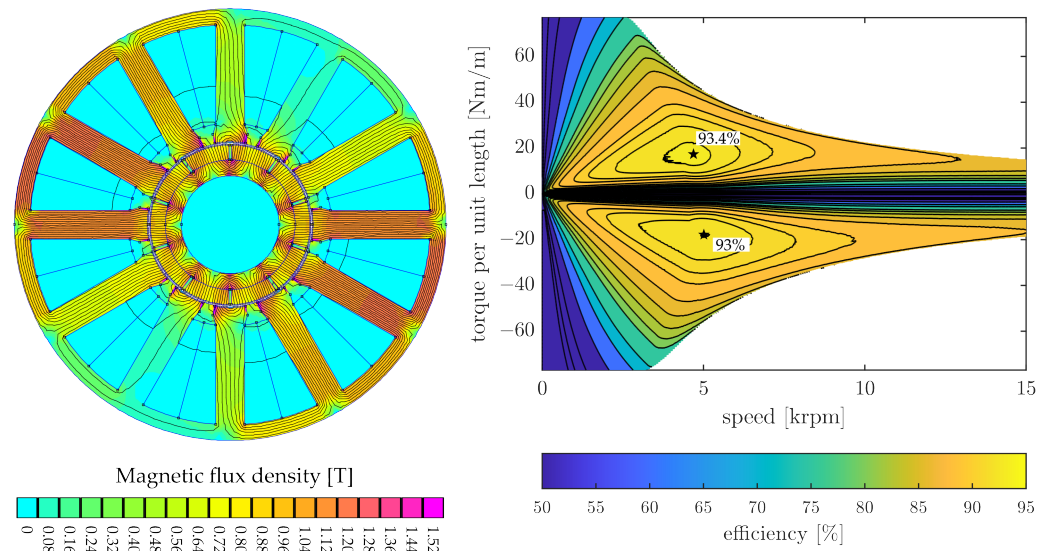


Figure 9. Left: Magnetic flux density map and out-of-plane magnetic vector potential contours for the SPM machine cross-section. Right: Efficiency map for the SPM machine over the first (motor) and fourth (generator) quadrants. Maximum efficiency values are highlighted (star).

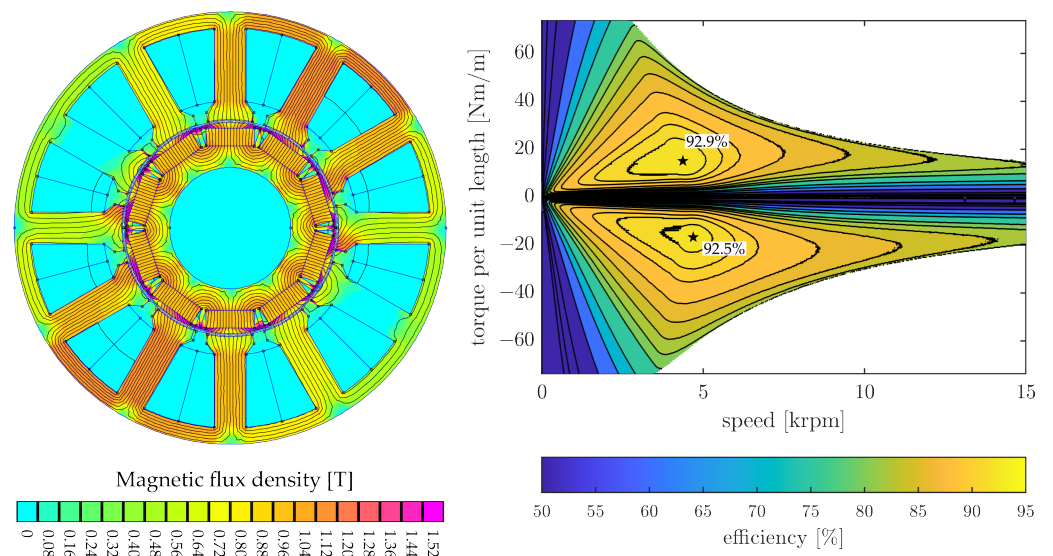


Figure 10. Left: Magnetic flux density map and out-of-plane magnetic vector potential contours for the IPM flat machine cross-section. Right: Efficiency map for the IPM flat machine over the first (motor) and fourth (generator) quadrants. Maximum efficiency values are highlighted (star).

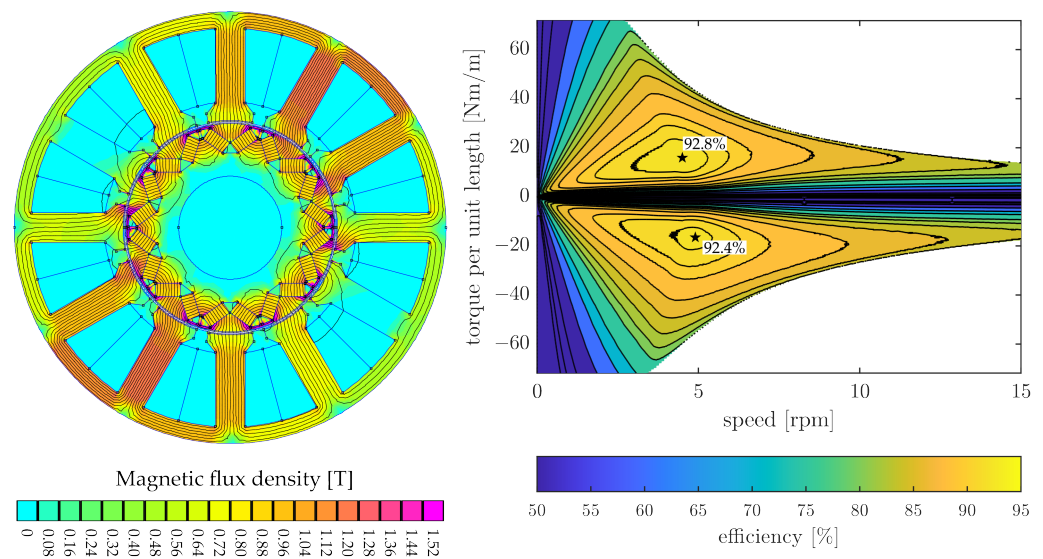


Figure 11. Left: Magnetic flux density map and out-of-plane magnetic vector potential contours for the IPM V-shape machine cross-section. Right: Efficiency map for the IPM V-shape machine over the first (motor) and fourth (generator) quadrants. Maximum efficiency values are highlighted (star).

Table 6. Quarter-car performance metrics with full active damping using three different PMSMs.

Metric	Units	SPM		IPM Flat		IPM V-Shape	
		Comfort	Road Holding	Comfort	Road Holding	Comfort	Road Holding
rms (a_w)	m/s ²	0.87	1.50	0.87	1.50	0.87	1.50
rms (η_{rh})	–	0.32	0.23	0.32	0.22	0.32	0.22
rms (F_a)	N	430.76	600.07	432.02	601.43	431.74	601.37
rms (T_m)	Nm	0.57	0.79	0.57	0.79	0.57	0.79
avg (P_m)	W	−95.98	−117.47	−96.43	−117.07	−96.34	−117.12
avg (P_{loss})	W	12.99	19.56	13.22	18.38	13.17	18.33
avg (P_e)	W	−82.99	−97.91	−83.20	−98.69	−83.17	−98.79
avg (η)	%	86.47	83.35	86.29	84.30	86.33	84.35
max ($ z_d $)	mm	45	27	45	27	45	27
max ($ \eta_{rh} $)	–	1.03	0.80	1.03	0.78	1.03	0.78

4. Conclusions

A design process was presented to find the parameters of a surface-mounted and two interior permanent magnets and to evaluate their performance in the presence of severe road conditions, actuator inertia, and friction.

The results showed that the surface-mounted machine is the most appropriate topology due to its high torque density, low torque ripple, and magnet mass. The dynamic vehicle performance, which was evaluated with the weighted chassis acceleration and road-holding index, is virtually equal in all designs. The three proposed machines fulfill actuator stroke and road-holding requirements. Indeed, the electric motor, on average, is self-sufficient from an energy standpoint: its maximum efficiency is found when operating in comfort mode.

Although the designed machines operate in the field-weakening region during transient periods, they mostly occupy the constant torque region. This finding suggests that it is more valuable to exploit the torque capability in the SPM than to exploit the field-weakening capability of IPM designs.

Future works will experimentally validate a motor prototype designed using the present process. Its performance will be evaluated when implemented in an active electromagnetic damper.

Author Contributions: Conceptualization, I.S.A.-Z. and R.G.; methodology, I.S.A.-Z., R.G. and L.I.; software, I.S.A.-Z.; validation, I.S.A.-Z.; formal analysis, I.S.A.-Z., R.G., L.I. and L.A.S.; investigation, I.S.A.-Z.; resources, N.A.; data curation, I.S.A.-Z.; writing—original draft preparation, I.S.A.-Z., R.G. and L.I.; writing—review and editing, N.A. and L.A.S.; visualization, I.S.A.-Z. and R.G.; supervision, R.G. and N.A.; project administration, R.G. and N.A.; funding acquisition, R.G. and N.A. All authors have read and agreed to the published version of the manuscript.

Funding: This research received no external funding.

Institutional Review Board Statement: Not applicable.

Informed Consent Statement: Not applicable.

Data Availability Statement: Data is unavailable due to privacy restrictions.

Conflicts of Interest: The authors declare no conflict of interest.

References

1. Chen, G.; Hua, M.; Liu, W.; Wang, J.; Song, S.; Liu, C. Planning and Tracking Control of Full Drive-by-Wire Electric Vehicles in Unstructured Scenario. *arXiv* **2023**, arXiv:2301.02753.
2. Ali, A.; Ahmed, A.; Ali, M.; Azam, A.; Wu, X.; Zhang, Z.; Yuan, Y. A review of energy harvesting from regenerative shock absorber from 2000 to 2021: Advancements, emerging applications, and technical challenges. *Environ. Sci. Pollut. Res.* **2023**, *30*, 5371–5406. [[CrossRef](#)] [[PubMed](#)]
3. Abdelkareem, M.A.; Xu, L.; Ali, M.K.A.; Elagouz, A.; Mi, J.; Guo, S.; Liu, Y.; Zuo, L. Vibration energy harvesting in automotive suspension system: A detailed review. *Appl. Energy* **2018**, *229*, 672–699. [[CrossRef](#)]
4. He, T.; Zhu, Z.; Eastham, F.; Wang, Y.; Bin, H.; Wu, D.; Gong, L.; Chen, J. Permanent Magnet Machines for High-Speed Applications. *World Electr. Veh. J.* **2022**, *13*, 18. [[CrossRef](#)]
5. Galluzzi, R.; Circosta, S.; Amati, N.; Tonoli, A. Rotary regenerative shock absorbers for automotive suspensions. *Mechatronics* **2021**, *77*, 102580. [[CrossRef](#)]
6. Amati, N.; Festini, A.; Tonoli, A. Design of electromagnetic shock absorbers for automotive suspensions. *Veh. Syst. Dyn.* **2011**, *49*, 1913–1928. [[CrossRef](#)]
7. Wang, J.; Geng, W.; Guo, J.; Li, L.; Zhang, Z. Design and Performance Comparison of Novel Flux-Concentrating IPM Machines for Power Generation System Application of Extended-Range Electric Vehicle. *IEEE Trans. Ind. Electron.* **2023**, *70*, 4450–4460. [[CrossRef](#)]
8. Genta, G.; Morello, L. *The Automotive Chassis: Volume 2: System Design*; Springer Nature: Berlin/Heidelberg, Germany, 2009.
9. Zuo, L.; Nayfeh, S. Low order continuous-time filters for approximation of the ISO 2631-1 human vibration sensitivity weightings. *J. Sound Vib.* **2003**, *265*, 459–465. [[CrossRef](#)]
10. 2631-1:1997; Mechanical Vibration and Shock—Evaluation of Human Exposure to Whole-Body Vibration—Part 1: General Requirements. International Organization for Standardization: Geneva, Switzerland, 1997.
11. Zuo, L.; Zhang, P.S. Energy Harvesting, Ride Comfort, and Road Handling of Regenerative Vehicle Suspensions. *J. Vib. Acoust.* **2013**, *135*, 011002. [[CrossRef](#)]
12. Dorrell, D.G.; Hsieh, M.F.; Popescu, M.; Evans, L.; Staton, D.A.; Grout, V. A Review of the Design Issues and Techniques for Radial-Flux Brushless Surface and Internal Rare-Earth Permanent-Magnet Motors. *IEEE Trans. Ind. Electron.* **2011**, *58*, 3741–3757. [[CrossRef](#)]
13. Bianchi, N.; Bolognani, S. Design techniques for reducing the cogging torque in surface-mounted PM motors. *IEEE Trans. Ind. Appl.* **2002**, *38*, 1259–1265. [[CrossRef](#)]
14. Magnussen, F.; Sadarangani, C. Winding factors and Joule losses of permanent magnet machines with concentrated windings. In Proceedings of the IEEE International Electric Machines and Drives Conference, IEMDC'03, Madison, WI, USA, 1–4 June 2003; Volume 1, pp. 333–339. [[CrossRef](#)]
15. Fonger, N. Metal Stamping Design Guidelines. Available online: http://larsontool.com/wp-content/uploads/2015/06/larson_design_guide.pdf (accessed on 15 February 2023).
16. Lu, C.; Ferrari, S.; Pellegrino, G. Two Design Procedures for PM Synchronous Machines for Electric Powertrains. *IEEE Trans. Transp. Electr.* **2017**, *3*, 98–107. [[CrossRef](#)]
17. Pellegrino, G.; Cupertino, F.; Gerada, C. Automatic Design of Synchronous Reluctance Motors Focusing on Barrier Shape Optimization. *IEEE Trans. Ind. Appl.* **2015**, *51*, 1465–1474. [[CrossRef](#)]
18. Meeker, D. Sliding Band Motion Model for Electric Machines. Available online: <https://www.femm.info/wiki/SlidingBand#> (accessed on 15 February 2023).
19. Hanselman, D.C. *Brushless Permanent-Magnet Motor Design*; McGraw-Hill, Inc.: New York, NY, USA, 1994.
20. Fatemi, A.; Demerdash, N.A.O.; Nehl, T.W.; Ionel, D.M. Large-Scale Design Optimization of PM Machines Over a Target Operating Cycle. *IEEE Trans. Ind. Appl.* **2016**, *52*, 3772–3782. [[CrossRef](#)]

21. Duan, Y.; Harley, R.; Habetler, T. Comparison of Particle Swarm Optimization and Genetic Algorithm in the design of permanent magnet motors. In Proceedings of the 2009 IEEE 6th International Power Electronics and Motion Control Conference, Wuhan, China, 17–20 May 2009; pp. 822–825. [CrossRef]
22. Duan, Y.; Ionel, D.M. A Review of Recent Developments in Electrical Machine Design Optimization Methods With a Permanent-Magnet Synchronous Motor Benchmark Study. *IEEE Trans. Ind. Appl.* **2013**, *49*, 1268–1275. [CrossRef]
23. Hanselman, D.C. *Brushless Permanent Magnet Motor Design*, 2nd ed.; The Writers' Collective: Cranston, RI, USA, 2003.
24. Soong, W.L.; Miller, T.J.E. Field-weakening performance of brushless synchronous AC motor drives. *IEE Proc.-Electr. Power Appl.* **1994**, *141*, 331–340. [CrossRef]
25. Meeker, D. Finite Element Method Magnetics/Version 4.2/User's Manual. Available online: <https://www.femm.info/wiki/Documentation/> (accessed on 15 February 2023).
26. Popescu, M.; Ionel, D.M.; Boglietti, A.; Cavagnino, A.; Cossar, C.; McGilp, M.I. A General Model for Estimating the Laminated Steel Losses Under PWM Voltage Supply. *IEEE Trans. Ind. Appl.* **2010**, *46*, 1389–1396. [CrossRef]
27. Ishak, D.; Zhu, Z.; Howe, D. Eddy-current loss in the rotor magnets of permanent-magnet brushless machines having a fractional number of slots per pole. *IEEE Trans. Magn.* **2005**, *41*, 2462–2469. [CrossRef]
28. Yang, Y.; Castano, S.M.; Yang, R.; Kasprzak, M.; Bilgin, B.; Sathyan, A.; Dadkhah, H.; Emadi, A. Design and Comparison of Interior Permanent Magnet Motor Topologies for Traction Applications. *IEEE Trans. Transp. Electrification* **2017**, *3*, 86–97. [CrossRef]
29. Plewa, K.M.; Eger, T.R.; Oliver, M.L.; Dickey, J.P. Comparison between ISO 2631—1 Comfort Prediction Equations and Self-Reported Comfort Values during Occupational Exposure to Whole-Body Vehicular Vibration. *J. Low Freq. Noise Vib. Act. Control.* **2012**, *31*, 43–53. [CrossRef]

Disclaimer/Publisher's Note: The statements, opinions and data contained in all publications are solely those of the individual author(s) and contributor(s) and not of MDPI and/or the editor(s). MDPI and/or the editor(s) disclaim responsibility for any injury to people or property resulting from any ideas, methods, instructions or products referred to in the content.